Shutterless ion mobility spectrometer with fast pulsed electron source

E. Bunert (iD), A. Heptner, T. Reinecke, A. T. Kirk (iD), and S. Zimmermann

View Online   Export Citation   CrossMark

ARTICLES YOU MAY BE INTERESTED IN

Shutterless ion mobility spectrometer with fast pulsed electron source

E. Bunert, A. Heptner, T. Reinecke, A. T. Kirk, and S. Zimmermann
Department of Sensors and Measurement Technology, Institute of Electrical Engineering and Measurement Technology, Leibniz Universität Hannover, Appelstr. 9a, 30167 Hannover, Germany

Ion mobility spectrometers (IMS) are devices for fast and very sensitive trace gas analysis. The measuring principle is based on an initial ionization process of the target analyte. Most IMS employ radioactive electron sources, such as ^{63}Ni or ^{3}H. These radioactive materials have the disadvantage of legal restrictions and the electron emission has a predetermined intensity and cannot be controlled or disabled. In this work, we replaced the ^{3}H source of our IMS with 100 mm drift tube length with our nonradioactive electron source, which generates comparable spectra to the ^{3}H source. An advantage of our emission current controlled nonradioactive electron source is that it can operate in a fast pulsed mode with high electron intensities. By optimizing the geometric parameters and developing fast control electronics, we can achieve very short electron emission pulses for ionization with high intensities and an adjustable pulse width of down to a few nanoseconds. This results in small ion packets at simultaneously high ion densities, which are subsequently separated in the drift tube. Normally, the required small ion packet is generated by a complex ion shutter mechanism. By omitting the additional reaction chamber, the ion packet can be generated directly at the beginning of the drift tube by our pulsed nonradioactive electron source with only slight reduction in resolving power. Thus, the complex and costly shutter mechanism and its electronics can also be omitted, which leads to a simple low-cost IMS-system with a pulsed nonradioactive electron source and a resolving power of 90. *Published by AIP Publishing.* [http://dx.doi.org/10.1063/1.4976021]

I. INTRODUCTION

Drift tube ion mobility spectrometers (IMS) can be used for the detection of trace gases by ionizing the analyte and separating the different ion species based on their drift time through a neutral gas under the influence of an electric field.[1] Commonly, the ionization is initiated by high kinetic energy electrons, emitted from a radioactive beta minus decay, such as from ^{3}H or ^{63}Ni. An ion shutter mechanism pushes the generated ions in a small packet into the drift region where the ions are separated. A small ion packet is necessary for the required resolving power and, respectively, the selectivity. For this purpose, a Bradbury-Nielsen shutter is typically used in many applications.[1,2] Alternatively, we employ a field switching shutter (FS) to realize ion mobility spectrometers with high analytical performance.[2] However, the disadvantages of radioactive electron sources are legal restrictions, complicating import, export, deployment in certain areas, and disposal of such devices. Furthermore, the electron emission can neither be controlled nor disabled. Therefore, the interest in nonradioactive alternatives has grown in recent years. Possible alternatives are, e.g., UV photo ionization lamps,[3,4] corona discharge,[5–7] X-ray sources,[8] or nonradioactive electron sources.[9,10] Unfortunately, the generated spectra by UV-photoionization and corona discharge differ from the spectra of a radioactive electron source, so they are not comparable.[3,6] X-ray sources generate comparable spectra but their disadvantage is a very high penetration depth. Therefore, setup modifications are required to prevent the additional ionization of the drift gas in the drift region.[8] Nonradioactive electron sources can provide several distinct advantages compared to their radioactive counterparts. No regulatory restrictions exist

and the experimental parameters, such as the emitted electron current or the kinetic energy of the electrons, can be controlled.

In addition, our electron source, which is based on thermionic electron emission, can be operated in a fast pulsed mode.[9] The short electron pulses with high intensity generate small ion packets at simultaneously high ion density, directly at the beginning of the drift region. This can be used for a source controlled injection, as described in Ref. 1, where the required initial small ion packet is generated by the pulsed electron source.

Thus, using a source controlled injection, a complex ion shutter mechanism, including necessary isolated, complex and therefore costly electronics, can be omitted. Although the control electronics of the nonradioactive electron source are still required, the major advantage of this setup is the simplified IMS design combined with less electronics compared to an IMS with a nonradioactive electron source and additional shutter. A first experiment in Ref. 9 has provided the proof of principle of this kind of shutterless IMS. In this work, we focus on the characterization and optimization of a shutterless IMS, via theoretical considerations supported by simulations and verification via measurements.

II. PRINCIPLE OF IMS AND NONRADIOACTIVE ELECTRON SOURCE

A. IMS with field switching ion shutter

Figure 1 shows a schematic of our conventional IMS with our nonradioactive electron source for ionization. The IMS can be separated in three sections: the ionization region between the electron source and the injection grid, the drift region
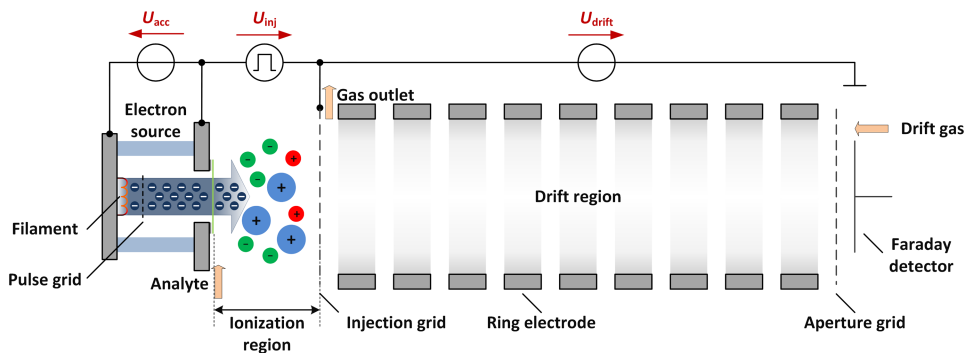
FIG. 1. Schematic of an IMS with field switching shutter and a nonradioactive electron source for ionization. The ionization process takes places in the ionization region. The generated ions can be injected as a small ion packet into the drift region by the injection voltage pulse U_{inj} with a shutter time of typically $t_{inj} = 20\,\mu s$.

between injection and aperture grid, and the Faraday detector. For analyzing trace gases, the analyte is injected into the ionization region. Here, the electron source initiates the atmospheric pressure chemical ionization (APCI) process. In the first step, reactant ions are generated from purified air. Subsequently, these reactant ions ionize the analyte molecules via proton transfer reaction.

Afterwards, the field switching shutter (FS) injects the generated ions into the drift region. The working principle of the FS is described in Ref. 2 and based on switching the injection voltage U_{inj} and thus the electrical field in the ionization region on and off, while the potential of the injection grid remains constant. During the shutter time of typically $t_{inj} = 20\,\mu s$, a significantly higher potential is applied to the electron source than that of the injection grid. Therefore, the ions are pushed into the drift region as a small ion packet. The advantages of the FS compared to the widely used Bradbury-Nielsen shutter are easier manufacturing of the mechanical parts, improved mechanical stability, and reduced distortion of the drift field.[2] The latter substantially influences the resolving power in compact drift tubes. To achieve a homogeneous electrical field in the drift region, the drift voltage of $U_{drift} = 5\,kV$ is applied via a resistive voltage divider to stainless steel ring electrodes separated by polyether ether ketone (PEEK) isolation rings. Accelerated by the drift field, the injected ion packet drifts towards the detector and thereby the different ion species are separated by their specific mobility in a neutral drift gas. Finally, the ions discharge on the Faraday detector and the resulting ion current is plotted over the drift time to obtain the ion mobility spectrum. The key for a high analytical performance is an efficient separation of the different ion species.[11] The resolving power R is a measure for the sharpness of a detected peak, which is described by Eq. (1).[1] A high resolving power is gained, when the full width at half maximum (FWHM) $w_{0.5}$ of the measured ion peaks is short compared to their drift time t_{drift},

$$R = \frac{t_{drift}}{w_{0.5}}. \qquad (1)$$

B. Nonradioactive electron source

The initial ionization of the analyte has a major impact on the achievable resolving power of a shutterless IMS. To investigate the influence of the ionization process on the generated ion distribution, the employed ionization source, i.e., the nonradioactive electron source, is described in this section. The

average kinetic electron energy of a ^3H source commonly used in IMS applications is about $E_{kin,^3H} = 5.7\,keV$.[12] To realize an electron source, generating electrons with comparable kinetic energies, we place a hot filament in a vacuum chamber to generate free electrons by thermionic emission. Subsequently, the electrons extracted from the hot filament are accelerated in a vacuum chamber by an acceleration voltage of up to $U_{acc} \leq 15\,kV$. At the end of the acceleration region, the vacuum chamber is sealed with a 300 nm thin Si_3N_4-membrane. Electrons with a kinetic energy of more than 5 keV can partially transmit through the membrane into the ionization region. The relative electron transmission and average kinetic energy of the electrons depend on the acceleration voltage, which is simulated with the Monte Carlo simulation software *Casino*, and shown in Figure 2.

For acceleration voltages of more than 8 kV, approximately 50% of the accelerated electrons can transmit through the membrane. After transmission, the electrons have an average kinetic energy of more than 4 keV. By simply varying the acceleration voltage of our electron source between 8 kV $\leq U_{acc} \leq 14\,kV$, the average kinetic energy of the emitted electrons can be adjusted. To reduce mechanical stress in the membrane, our electron source typically operates at $U_{acc} = 10\,kV$, leading to emitted electrons with an average kinetic energy of $E_{kin} = 7.2\,keV$, which is comparable to a radioactive ^3H-source.[9,10,12,13] A major advantage of our nonradioactive electron source is that the electron emission current is adjustable from a few tens of picoamperes (which is
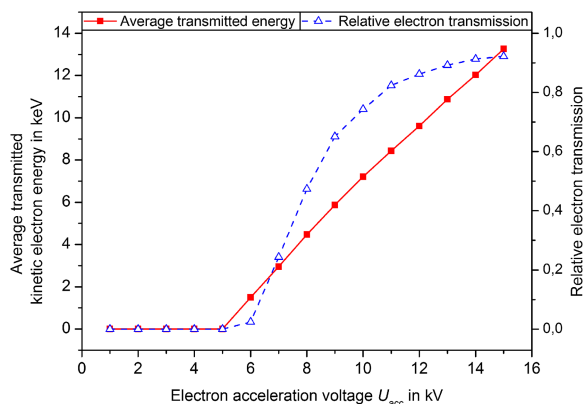

FIG. 2. Simulation results for relative transmission of high kinetic electrons through a 300 nm thin Si_3N_4-membrane (a) and simulation results for average kinetic electron energy after transmitting through a 300 nm thin Si_3N_4-membrane (b).

TABLE I. Electron source operating parameters.

Parameter	Value
Si_3N_4 membrane thickness	300 nm
Si_3N_4 membrane diameter	1.5 mm × 1.5 mm
Electron acceleration voltage U_{acc}	8 . . . 14 kV
Corresponding kinetic electron energies after transmission through Si_3N_4 membrane	4.5 . . . 12 keV
Filament current	200 . . . 270 mA
Emission current	0.2 . . . 100 nA
Grid voltage low	−120 V
Grid voltage high	25 V
Electron pulse width/ionization time t_{ion}	100 ns . . . ∞
Absolute pressure inside the vacuum chamber	$2 \cdot 10^{-7}$ hPa

TABLE II. IMS operating parameters.

Parameter	Value
Drift length l_{drift}	100 mm
Drift region diameter	15 mm
Repetition rate	40 Hz
Drift voltage U_{drift}	5 kV
Aperture voltage	100 V
Electrical field in the drift region E_{drift}	50 . . . 100 V/mm
Electrical field in the ionization region E_{ion}	100 . . . 2500 V/mm
Drift gas flow	160 mls/min
Sample gas flow	10 mls/min
Dew point drift gas and sample carrier	−89 °C
Operating pressure	1018 mbar
Operating temperature	25 °C

comparable to the electron emission of a tritium source with 300 MBq) up to hundreds of nanoamperes.

To operate the electron emitter in pulsed mode,[9] we place a grid in front of the hot filament for switching the electron beam passing through the silicon nitride membrane. By optimizing the geometric parameters and the control electronics, we can achieve electron pulses with a definable pulse width of down to a few nanoseconds, whereby the emission current can still be adjusted in the range mentioned above. The operating parameters of the electron source used in this work are listed in Table I.

C. Shutterless IMS with pulsed electron source

The design of the shutterless IMS is similar to our conventional IMS design. The biggest difference is that there is no restricted ionization region anymore. This leads to a combined drift and ionization region where the ionization takes place at the beginning of the drift region, as shown in Figure 3. The second part of the drift region is the actual drift region, where the generated ion species are separated. For a modular experimental setup, the electrical fields in the ionization region E_{ion} and in the actual drift region E_{drift} are adjustable by two independent voltage sources $U_{E,ion}$ and U_{drift} (Figure 3).

The drift tube used in this work is based on the drift tube described in Refs. 14 and 15 with a drift length of l_{drift} = 100 mm. The IMS operating parameters are listed in Table II.
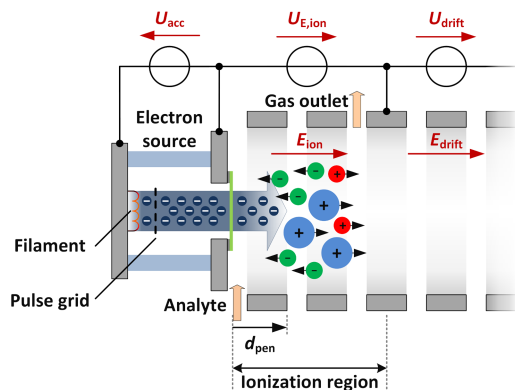

FIG. 3. Ionization scheme of a shutterless IMS with pulsed electron source. The short electron pulse generates a small ion packet in the ionization region as a part of the drift region. The generated ions are subsequently accelerated by the adjustable electrical field E_{ion} towards the detector.

Note that the IMS in Refs. 14 and 15 use significant different parameters compared to the IMS described in this work (e.g., a higher drift voltage). Therefore, the analytical performance of those setups is not directly comparable. The electrical field of the ionization region is limited to the first 3 mm of the drift region. The control electronics for the shutterless IMS and the electron source as well as the data recording electronics and software are self-developed for this application. Only the drift voltage U_{drift} is generated by a power supply from FuG. For the drift and sample carrier gas, purified and dried air is used.

III. ION GENERATION

A. Electron penetration depth

As the ionization region is located directly at the beginning of the drift tube, the ions are generated in a region with a constant electrical field E_{ion}. Therefore, the ions are directly accelerated towards the detector (ions with opposite polarity are accelerated towards the electron source, respectively). Regarding the resolving power of the IMS, described by Eq. (1), there are two major influences on the width of the initial ion packet. As the ions are immediately accelerated towards the detector, the first major influence is the ionization time, which directly adds to the ion packet width in the time domain. Second, the minimum spatial width of the initial ion packet is determined by the penetration depth d_{pen} of the electrons emitted into the ionization region.

It is obvious that the penetration depth directly depends on the kinetic energy $E_{kin,el}$ of the emitted electrons and thus on the electron acceleration voltage U_{acc}. The resulting penetration depth d_{pen} of the electrons into dry air and the energy deposition in the ionization region are simulated with *Casino* as function of the kinetic electron energy. Approximately, the deposited energy is proportional to the ion production rate. Plotting the simulation results over the penetration depth, the generated ion densities are illustrated as a function of the distance to the electron source in Figure 4 for three exemplary acceleration voltages U_{acc}.

The simulation results show that both the ion density and the spatial width of the ion distribution increase towards higher kinetic electron energies. This results in a wider
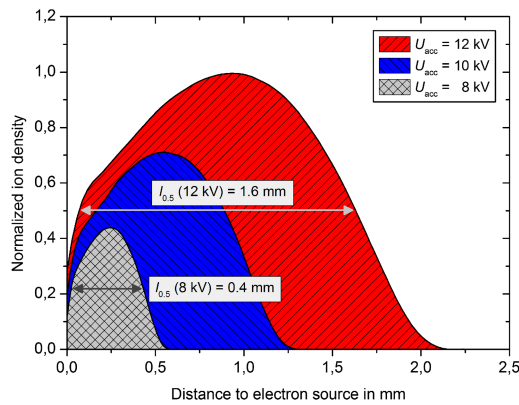
FIG. 4. Simulated normalized ion density as a function of the distance to the electron source for electron acceleration voltages of 8 kV, 10 kV, and 12 kV.

ionization region and thus in broadened initial ion packets. While higher ion concentrations improve the sensitivity, wider spatial widths reduce the resolving power of an IMS. Therefore, a compromise must be achieved between high sensitivity and high resolving power by optimizing the parameters.

To investigate the influence of the acceleration voltage on the generated ion distribution, the positive reactant ion peak (RIP$^+$), generated by ionizing purified dry air, is measured for different acceleration voltages between 8 kV and 14 kV. Hereby, the ionization pulse width is set to a constant value of $t_{ion} = 10$ μs. Furthermore, the emission current (i.e., intensity) of the electron source is adjusted for each acceleration voltage to achieve a constant RIP$^+$ amplitude of 100 pA. The electrical field in both the drift region and the ionization region is set to $E_{ion} = E_{drift} = 50$ V/mm. Figure 5 shows three examples for the resulting RIP$^+$ for 8 kV, 10 kV, and 12 kV acceleration voltages.

As can be expected from the simulation results in Figure 4, the center of the detected RIP$^+$ shifts to shorter drift times with increasing acceleration voltages. Furthermore, the FWHM $w_{0.5}$ of the detected RIP$^+$ increases with higher kinetic electron energies from 158 μs at $U_{acc} = 8$ kV to 183 μs at $U_{acc} = 12$ kV because of the higher penetration depth of the electrons. It is noticeable that the spatial FWHM ratio between the simulated distributions at $U_{acc} = 12$ kV and $U_{acc} = 8$ kV is 4, but

the temporal FWHM ratio of the detected RIP$^+$s is only about 1.16. This can be explained by broadening influences during the drift towards the detector, such as diffusional broadening or Coulombic repulsion. Therefore, a detailed investigation is performed in Sec. III B to describe the relations between the initial ion packet and the detected peaks.

B. Initial ion packet width and maximum attainable resolving power

In this section, the influence of the initial spatial width on the temporal FWHM $w_{0.5}$ of the RIP$^+$ and thus on the resolving power is investigated. Therefore, the resulting initial FWHM w_{init} in the time domain is calculated with Eq. (2). The spatial FWHM $l_{0.5}$ for various acceleration voltages is derived from the ion distribution depicted in Figure 4. Furthermore, the drift velocity v of the ions is required. It is found by multiplication of the ion mobility K of an ion species and the electrical field E. As a result of numerous measurements, we specified the ion mobility of the positive reactant ions to $K_{RIP} = 2.31$ cm^2/Vs at 25 °C,

$$w_{init} = \frac{l_{0.5}}{v} = \frac{l_{0.5}}{K \cdot E}. \tag{2}$$

Figure 6 depicts the initial ion FWHM w_{init}, derived from Eq. (2) for various electrical fields E_{ion} and acceleration voltages U_{acc}. These results illustrate the relevance of the electrical field E_{ion} in the ionization region for the initial time domain FWHM w_{init}, particularly at high acceleration voltages and high penetration depths, respectively. The results show that the combination of the lowest acceleration voltage and highest electrical field leads to the smallest w_{init} and thus to the highest possible resolving power of the IMS.

For calculating the resulting FWHM of the reactant ion peak (RIP$^+$) $w_{0.5}$, the relation between the initial FWHM w_{init} and $w_{0.5}$ can be approached by Eq. (3) as a geometrical addition of the initial width of the ion packet w_{init}, additional broadening influence of the amplifier w_{amp}, the diffusional broadening w_{diff}, and the Coulombic broadening w_{coul}:[11,14,16]

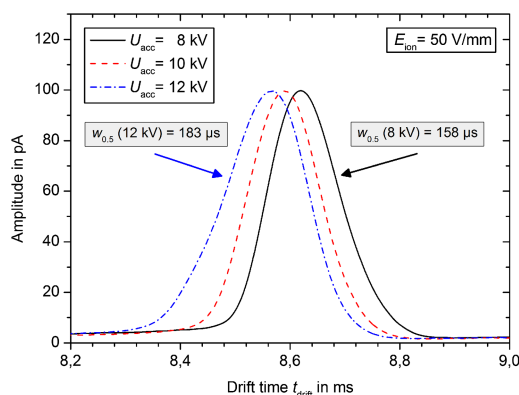$$w_{0.5} = \sqrt{w_{init}^2 + w_{diff}^2 + w_{coul}^2 + w_{amp}^2}. \tag{3}$$

FIG. 5. Broadening of the detected RIP$^+$ with increased acceleration voltage and thus increased penetration depth of the electrons. The electrical field in the ionization region and the drift region is $E_{ion} = E_{drift} = 50$ V/mm, the ionization time is set to 10 μs.
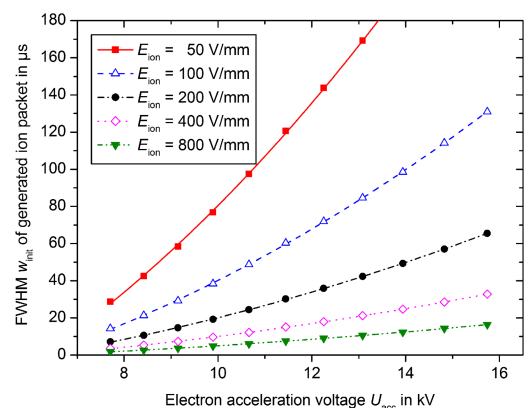

FIG. 6. Resulting initial FWHM w_{init} in the time domain, based on Figure 4, as a function of the acceleration voltage U_{acc} for various electrical fields E_{ion} in the ionization region. The associated ion mobility for the reactant ions at room temperature is $K_{RIP} = 2.31$ cm^2/Vs.
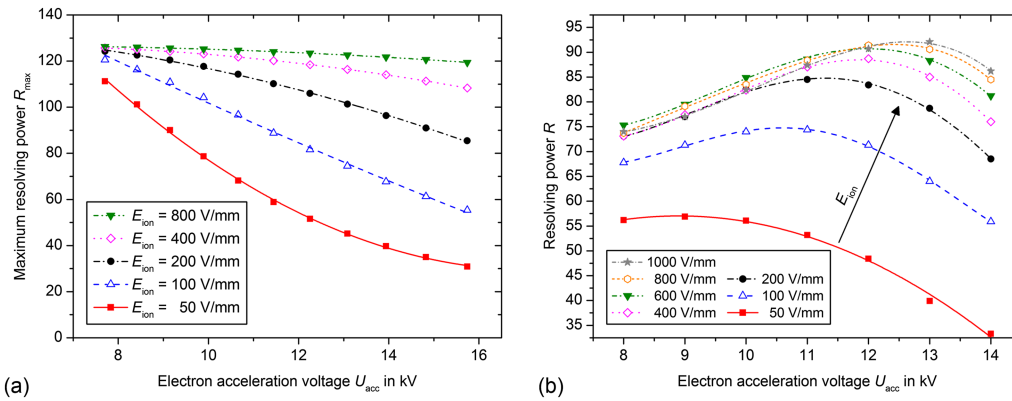
FIG. 7. Calculated (a) and measured (b) maximum resolving power (of the RIP$^+$) as a function of the acceleration voltage U_{acc} and the electrical field E_{ion}, in the ionization region based on the resulting initial FWHM w_{init} in the time domain of Figure 6 and Eq. (6). The used parameters are drift voltage U_{drift} = 5 kV, drift length l_{drift} = 100 mm, ion mobility K_{RIP} = 2.31 cm^2/Vs, temperature T = 298.15 K, ionization time t_{ion} = 10 μs. The RIP$^+$ amplitude is controlled to a constant value of 100 pA.

For low ion densities, the Coulombic broadening term w_{coul} can be neglected, as it is relatively small and the resulting FWHM is dominated by the remaining broadening terms. The influence of the amplifier previously was determined to w_{amp} = 17 μs.[15] The diffusional broadening w_{diff} is described by Eq. (4) as a function of the drift voltage U_{drift} and the drift time t_{drift},[11,17,18]

$$w_{diff} = \left(\frac{16\,k_B\,T\,\ln 2}{e\,U_{drift}} \right)^{\frac{1}{2}} t_{drift}. \qquad (4)$$

The injection width of the initial ion packet for this IMS configuration but with a field switching ion shutter is specified in Ref. 15 as w_{init} = 5...20 μs. Therefore, we set the electron pulse width to t_{ion} = 10 μs for the first investigation of the shutterless configuration. As mentioned above, this time directly adds to the initial time domain FWHM w_{init} because of the immediate acceleration of the generated ions in the shutterless ionization region. This leads to an extended formulation of Eq. (3) for the minimum FWHM of the measured RIP$^+$ $w_{0.5}$,

$$w_{0.5} = \sqrt{(w_{init} + t_{ion})^2 + w_{diff}{}^2 + w_{amp}{}^2}. \qquad (5)$$

Insertion of Eqs. (2), (4) and (5) in Eq. (1) yields the following expression for the maximum attainable resolving power R_{max}:

$$R_{max} \leq \frac{t_{drift}}{w_{0.5}}$$

$$= \frac{\frac{l_{drift}{}^2}{K \cdot U_{drift}}}{\sqrt{\left(\frac{l_{0.5}}{K \cdot E_{ion}} + t_{ion} \right)^2 + \frac{16\,k_B\,T\,\ln 2}{e \cdot U_{drift}} \cdot \left(\frac{l_{drift}{}^2}{K \cdot U_{drift}} \right)^2 + w_{amp}{}^2}}. \qquad (6)$$

With Eq. (6) and the results of Figure 6, we can calculate the maximum resolving power as a function of the acceleration voltage U_{acc} and the electrical field E_{ion} in the ionization region, which is plotted in Figure 7(a). The related parameters are listed in the caption. These results indicate that the highest possible resolving power requires a low acceleration voltage and a high electrical field in the ionization region.

Figure 7(b) shows the measuring results corresponding to the theoretical considerations in Figure 7(a). Here, the resolving power of the measured RIP$^+$ is plotted over the acceleration

voltage for various electrical fields in the ionization region. The measurement results show that there is a maximum resolving power for each electrical field. However, in contrast to the calculation results, the maximum is not found at the lowest acceleration voltage. For example, the plot for an electrical field of E_{ion} = 100 V/mm shows a local maximum at U_{acc} = 10.6 kV with a resolving power of R = 74.8. The deviation between calculation and measurement can be explained by the negligence of the Coulomb broadening w_{coul}. For lower acceleration voltages, the intensity of the electron source has to be dramatically increased, in order to generate RIP$^+$ amplitudes equal to the amplitudes for high acceleration voltages at the same ionization time. Therefore, Coulombic repulsion increases because of the increased ion density and becomes the major broadening influence on $w_{0.5}$ (see Eq. (3)) and hence on the resulting resolving power. Thus, the resolving power is not a constantly increasing towards lower penetration depths, as suggested by the simulation results in Figure 6. Instead, the resolving power shows a maximum value at a certain acceleration voltage for each electrical field in the ionization region. These voltages and their corresponding electrical field E_{ion} and resolving power R are shown in Table III.

C. Ionization time

The preceding measurements were carried out with an ionization time of t_{ion} = 10 μs. As this time directly adds to the initial width w_{init} of the ion packet, the influence of t_{ion} on the resolving power is investigated in this section. Hereby, the electrical field E_{ion} in the ionization region is set to different values between 50 V/mm and 1000 V/mm, while the

TABLE III. Optimum acceleration voltages $U_{acc,opt}$ at different electrical fields E_{ion} in the ionization region.

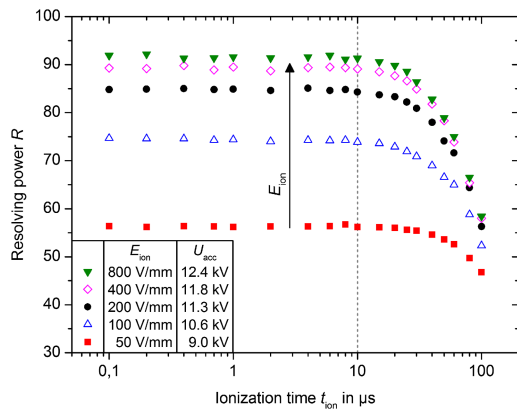| E_{ion} in V/mm	$U_{acc,opt}$ in kV	R	E_{ion} in V/mm	$U_{acc,opt}$ in kV	R
50	9.0	56.9	600	12.0	90.7
100	10.6	74.8	800	12.4	91.6
200	11.3	84.8	1000	12.6	92.0
400	11.8	88.5			

FIG. 8. Resolving power R over ionization time t_{ion} for different electrical fields E_{ion} in the ionization region. The acceleration voltage U_{acc} is always adjusted to the related optimum value, the RIP$^+$ amplitude is controlled to a constant value of 100 pA, the electrical field in the drift region is $E_{drift} = 50$ V/mm.

acceleration voltage is adjusted to the previously determined corresponding optimum (see Table III). Figure 8 shows the measured resolving power R of the RIP$^+$ with a constant amplitude of 100 pA as a function of the ionization time t_{ion}. A decreasing resolving power can be observed for ionization times longer than $t_{ion} > 10 \ \mu s$ because of the direct broadening of the initial ion packet, described in Eqs. (5) and (6), respectively.

However, ionization times shorter than $t_{ion} \leq 10 \ \mu s$ do not lead to an improvement of the resolving power. This is attributed to an increased Coulombic repulsion with shorter ionization times, as the intensity of the electron source has to be increased to generate the same quantity of ions to reach equal RIP$^+$ amplitudes for all measurements. Furthermore, the influence of the remaining broadening terms dominates the width of the ion packet towards very short ionization times. However, with regard to the reachable minimum limit of detection (LoD) a longer ionization time is favorable. Therefore, the highest possible ionization time without reduction of the resolving power is selected and thus the reaction time for generating the analyte ions is increased.

D. Limit of detection

Beside the resolving power, the limit of detection (LoD) of an IMS describes its analytical performance. For a preliminary characterization of our setup, we use acetone as analyte, purchased from Sigma Aldrich. The acetone is filled in a vial heated to 35 °C in a permeation oven. For generating a constant acetone vapor concentration, the oven is purged with a constant flow of 600 mls/min of purified dry air. An adjustable fraction of this gas is diluted with dry air for generating different acetone concentrations in the sample gas.

For all measurements, we set the ionization time to 10 μs. The drift voltage is set to $U_{drift} = 5$ kV, and the electrical field E_{ion} in the ionization region is varied between 100 V/mm and 800 V/mm. Hereby, the acceleration voltage is set to its optimum value (see Table III). Furthermore, the RIP$^+$ amplitude is kept constant at 100 pA without analyte. As the RIP$^+$ amplitude

TABLE IV. Total ion charge for different electrical fields E_{ion} in the ionization region with a constant RIP$^+$ amplitude of 100 pA, without analyte.

E_{ion} in V/mm	100	200	400	800
Q_{tot} in fC	12.3	10.6	9.9	9.6

cannot be used as a measure for the source activity when measuring a gas mixture, the total ion charge Q_{tot} of the detected spectrum is determined. The results are shown in Table IV.

Adjusting the total ion charge for every E_{ion} by adjusting the filament current ensures a constant electron emission of the electron source and thus a constant ion quantity for all measurements. Figure 9 shows an exemplary spectrum of the shutterless IMS for an acetone concentration of 20 ppb$_v$. The related parameters are listed in the caption.

Subsequently, we determined the LoD for different E_{ion} based on the measured noise of the baseline and the measured linear amplitude increase of the acetone monomer peak at low concentrations. The LoD is defined as three times the standard deviation of the noise. The determined LoDs for a measuring time of 1 s are listed in Table V. The respective resolving power R of the RIP$^+$ without analyte in the ionization region is also listed in this table as a reminder. For the maximum reachable resolving power of $R = 92$ at $E_{ion} = 800$ V/mm we achieve a LoD for acetone of about 4 ppb$_v$. This can be slightly improved to ≈ 2 ppb$_v$ by reducing the electrical field to $E_{ion} = 100$ V/mm and hence increasing the reaction time, but with a slightly decreased resolving power of $R = 75$.

For comparison, the corresponding LoD$_{FS}$ and resolving power R_{FS} of this IMS equipped with field switching shutter and an ionization time of $t_{ion} = 10 \ \mu s$ is about LoD$_{FS} = 1$ ppb$_v$ at $R_{FS} = 92$. Therefore, we reach nearly the same LoD for acetone as with the shutterless IMS at low electrical fields E_{ion} in the ionization region. The resolving power R_{FS} is comparable to that one of the shutterless IMS at high E_{ion}. This suggests that we found the parameters for the best achievable LoD at the highest possible resolving power with this shutterless IMS. Depending on the application, the focus can be set on either a low LoD or a high resolving power only by adjusting the electrical field E_{ion} in the ionization region.
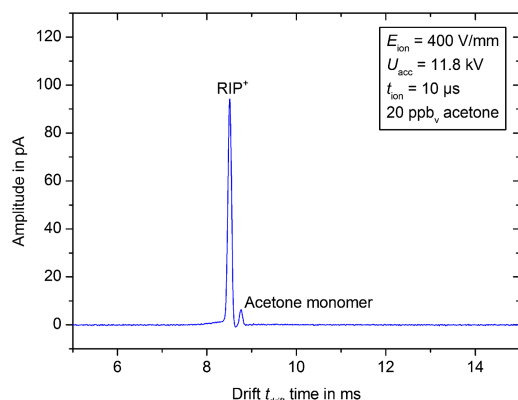

FIG. 9. Positive shutterless-IMS-spectrum of 20 ppb$_v$ acetone in clean dry air. The drift voltage is set to $U_{drift} = 5$ kV. The total ion charge is controlled to a constant value of $Q_{tot} = 9.9$ fC.

TABLE V. Limit of detection for acetone in 1 s at different electrical fields E_{ion} and an ionization time of 10 μs. The total ion charge is controlled to the constant value at a RIP$^+$ amplitude of 100 pA without acetone. The comparable LoD for acetone in an IMS with field switching shutter (FS) ($t_{ion} = 10\,\mu$s, $t_{FS} = 100\,\mu$s) is LoD$_{FS}$ = 1 ppb$_v$ at R_{FS} = 92.

E_{ion} in V/mm	$U_{acc,opt}$ in kV	LoD in ppb$_v$	R
100	10.6	1.8 ($\pm$1)	75
200	11.3	2.5 ($\pm$1)	85
400	11.8	3.5 ($\pm$1)	89
800	12.4	4.2 ($\pm$1)	92

IV. CONCLUSION

In this paper, we presented the realization and investigation of a shutterless IMS with a pulsed, nonradioactive electron source for initial ionization. With sufficiently short electron emission pulses with adjustable intensity, our nonradioactive electron source can generate small initial ion packets for a subsequent separation in the drift region. Therefore, a separated ion shutter mechanism is not required. For the investigation of the influence of different parameters on the analytical performance of this shutterless IMS, we first simulated the electron penetration depth into dry air for various electron acceleration voltages. With this result, we estimated the corresponding generated ion distribution in the ionization region. To generate an equal total ion charge at low electron acceleration voltages and hence at lower penetration depths, it is obvious that the ion density has to be drastically increased. This implies an increasing broadening influence by Coulombic repulsion. However, at high electron acceleration voltages, the penetration depth and thus the initial width of the ion packet is increased which implies high electrical fields in the ionization region. Both reduce the resolving power and therefore the analytical performance of this kind of IMS. By appropriate measurements, we found for each electrical field E_{ion} in the ionization region an optimum acceleration voltage for the highest possible resolving power. However, for electrical fields above $E_{ion} \geq$ 800 V/mm or ionization times below $t_{ion} \leq$ 10 μs, no further significant improvement of the resolving power can be observed. Finally, the limit of detection for acetone was determined to 4.2 ppb$_v$ at an electrical field of E_{ion} = 800 V/mm and a resolving power of R = 92. This can be improved down to 1.8 ppb$_v$ by reducing the electrical field to E_{ion} = 100 V/mm accepting a decreased resolving power of R = 75. These limits of detection are comparable to a conventional IMS with identical ionization times. One particular advantage of this shutterless IMS is that a choice can be made between a better limit of detection and a higher resolving power, almost exclusively by varying the electrical field in the ionization region.

[1]G. A. Eiceman, Z. Karpas, and H. H. Hill, *Ion Mobility Spectrometry*, 3rd ed. (CRC Press, Boca Raton, 2013).

[2]A. T. Kirk and S. Zimmermann, "Bradbury-Nielsen vs. field switching shutters for high resolution drift tube ion mobility spectrometers," Int. J. Ion Mobility Spectrom. **17** (3-4), 131–137 (2014).

[3]J. I. Baumbach, S. Sielemann, Z. Xie, and H. Schmidt, "Detection of the gasoline components methyl tert -butyl ether, benzene, toluene, and m -xylene using ion mobility spectrometers with a radioactive and UV ionization source," Anal. Chem. **75**(6), 1483–1490 (2003).

[4]St. Sielemann, J. I. Baumbach, H. Schmidt, and P. Pilzecker, "Detection of alcohols using UV-ion mobility spetrometers," Anal. Chim. Acta **431**(2), 293–301 (2001).

[5]H. Borsdorf, "Determination of n-alkanes and branched chain alkanes by Corona discharge ion mobility spectrometry," Int. J. Ion Mobility Spectrom. **2**, 9–14 (1999).

[6]C. L. Crawford and H. H. Hill, "Comparison of reactant and analyte ions for ^{63}Nickel, corona discharge, and secondary electrospray ionization sources with ion mobility-mass spectrometry," Talanta **107**, 225–232 (2013).

[7]G. A. Eiceman, J. H. Kremer, A. P. Snyder, and J. K. Tofferi, "Quantitative assessment of a corona discharge ion source in atmospheric pressure ionization-mass spectrometry for ambient air monitoring," Int. J. Environ. Anal. Chem. **33** (3-4), 161–183 (1988).

[8]T. Reinecke, A. T. Kirk, A. Heptner, D. Niebuhr, S. Bottger, and S. Zimmermann, "A compact high-resolution x-ray ion mobility spectrometer," Rev. Sci. Instrum. **87**(5), 53120 (2016).

[9]P. Cochems, A. T. Kirk, E. Bunert, M. Runge, P. Goncalves, and S. Zimmermann, "Fast pulsed operation of a small non-radioactive electron source with continuous emission current control," Rev. Sci. Instrum. **86**(6), 65102 (2015).

[10]P. Cochems, M. Runge, and S. Zimmermann, "A current controlled miniaturized non-radioactive electron emitter for atmospheric pressure chemical ionization based on thermionic emission," Sens. Actuators, A **206**, 165–170 (2014).

[11]A. B. Kanu, M. M. Gribb, and H. H. Hill, "Predicting optimal resolving power for ambient pressure ion mobility spectrometry," Anal. Chem. **80**(17), 6610–6619 (2008).

[12]F. T. Porter, "Beta decay energy of tritium," Phys. Rev. **115**(2), 450–453 (1959).

[13]A. Morozov, T. Heindl, C. Skrobol, J. Wieser, R. Krücken, and A. Ulrich, "Transmission of ~10 keV electron beams through thin ceramic foils: Measurements and Monte Carlo simulations of electron energy distribution functions," Eur. Phys. J. D **48**(3), 383–388 (2008).

[14]A. T. Kirk, M. Allers, P. Cochems, J. Langejuergen, and S. Zimmermann, "A compact high resolution ion mobility spectrometer for fast trace gas analysis," Analyst **138**(18), 5200–5207 (2013).

[15]A. T. Kirk and S. Zimmermann, "An analytical model for the optimum drift voltage of drift tube ion mobility spectrometers with respect to resolving power and detection limits," Int. J. Ion Mobility Spectrom. **18** (3-4), 129–135 (2015).

[16]A. V. Tolmachev, B. H. Clowers, M. E. Belov, and R. D. Smith, "Coulombic effects in ion mobility spectrometry," Anal. Chem. **81**(12), 4778–4787 (2009).

[17]W. F. Siems, C. Wu, E. E. Tarver, H. H. Hill, Jr., P. R. Larsen, and D. G. McMinn, "Measuring the resolving power of ion mobility spectrometers," Anal. Chem. **66**(23), 4195–4201 (1994).

[18]H. E. Revercomb and E. A. Mason, "Theory of plasma chromatography/gaseous electrophoresis. Review," Anal. Chem. **47**(7), 970–983 (1975).